

Article

Corrosion Performance of Commercial Alloys and Refractory Metals in Conditions for Electrorefining of Spent Nuclear Fuels

Yanhong Jia¹, Shuangshuang Chang², Xin Du², Shaoqiang Guo^{2,*}

¹ China Institute of Atomic Energy, Beijing 102413, P.R. China

² School of Nuclear Science and Technology, Xi'an Jiaotong University, Xi'an 710049, P.R. China

* Correspondence: guos2019@mail.xjtu.edu.cn

Abstract: Molten LiCl-KCl salt and liquid cadmium are proposed as the electrolyte and the reactive cathode for the electrorefining of spent nuclear fuels. Corrosion testing of existing alloys is mandatory to ensure the service life of the electrorefiner vessel and electrode assemblies. Haynes C276, Inconel 600, AISI 316L stainless steel, and 42CrMo low alloy steel were exposed to LiCl-KCl melt at 500°C for 500 h in an argon atmosphere. All alloys suffered from dissolution attacks with the presence of oxide islands or porous oxide layer on the surface. AISI 316L, T91 steel and tungsten specimens were also submitted to corrosion tests in liquid cadmium at 500°C for 120 h. Corrosion of AISI 316L and T91 stainless steel were predominated by chemical oxidation with additional severe Ni dealloying occurred on AISI 316L. Tungsten only suffered from dissolution attack in comparison.

Keywords: Corrosion, Molten salts, Liquid cadmium, SEM.

1. Introduction

Pyroprocessing is an alternative approach to the conventional hydrometallurgy process for the reprocessing of spent nuclear fuels (SNFs), which is more compatible with the fast reactor fuel cycle. The key step of the pyroprocessing is the electrorefining of uranium in LiCl-KCl molten salt. In this step, uranium and transuranic elements in the SNF are dissolved in the molten salt and selectively recovered on the solid cathode and liquid cadmium cathode, respectively [1].

However, the structural alloys used for construction of the electrorefiner vessel and electrode assemblies may suffer corrosion attack. In general, molten chloride salts can cause corrosion of alloys by the active dissolution of the alloy constituents, selective attack, pitting, intergranular corrosion, and oxidation [2]. It is known that the traditional corrosion resistant alloys rely on the formation of passive oxide film on the alloy surface in aqueous solutions. However, the formation of protective oxide film is typically challenging in molten chloride media which makes the active dissolution play a more pronounced role compared to the aqueous environment. The presence of dissolved actinide and fission products during the electrorefining can also accelerate the dissolution kinetics of alloy elements in the molten salt electrolyte [3-5]. There are only very limited studies that have investigated the corrosion resistance of existing alloys in molten LiCl-KCl salts [6-9]. Most of these studies deduced that corrosion rate only becomes pronounced in reactive atmosphere. Our previous study also showed quite low corrosion rate of commercial alloys including Haynes C276, Inconel 600, Incoloy 800, and 316L stainless steel in molten LiCl-KCl under inert atmosphere during a test duration of 24 h [10]. However, to ensure the adequate vessel integrity through entire design life typically 40 years, there is a need to further evaluate the corrosion performance of existing alloys in molten salt for long-term exposure. Moreover, the electrorefiner vessel, cathode assemblies and agitators are also in contact with the liquid cadmium. The solubility of alloying elements such as Ni is more than 10 at% in liquid cadmium at 500°C [11]. This is much higher than their solubilities in liquid lead and lead-bismuth eutectic [12]. In fact, as a promising candidate

coolant for future nuclear reactors, the corrosion dissolution and the resulted embrittlement problems of structure alloys in liquid lead and lead-bismuth eutectic have been well aware of and extensively studied in the past two decades [13,14]. Few studies have been undertaken on the corrosion behaviors of alloys in liquid cadmium.

Therefore, the objective of this study is to find materials with better corrosion resistance in molten LiCl-KCl salt and liquid cadmium. Corrosion tests of several representative alloys and refractory metals will be carried out in an argon atmosphere to evaluate the corrosion performance.

2. Materials and Methods

The nominal chemical compositions of the materials tested in the present study are shown in Table 1. Haynes C276, Inconel 600, AISI 316L, T91, 42CrMo steel and tungsten (99.99 purity) were cut into dimension of 15 mm × 5 mm × 2 mm for corrosion testing. All specimens were ground up to 1500 grit SiC papers, then polished with 0.3 μm alumina polishing agent. Prior to testing, alloy specimens were cleaned with acetone, deionized water, ethanol, and then dried.

Table 1. Chemical composition of the tested alloys (wt%).

| Materials | Cr | Fe | Ni | Mo | Si | W | Mn | Al | V | Cu | C | Others |
|-------------|-------|------|-------|-------|-------|------|-------|-------|-------|-------|-------|----------|
| Haynes C276 | 16.17 | 6.22 | Bal. | 16.08 | – | 3.21 | – | 0.28 | 0.081 | 0.079 | – | Co 0.067 |
| Inconel 600 | 15.72 | 9.90 | Bal. | – | 0.118 | – | 0.396 | | | 0.11 | 0.024 | – |
| AISI 316L | 16.3 | Bal. | 10.15 | 2.57 | 0.48 | – | 0.97 | | | | 0.015 | – |
| T91 | 9.47 | Bal. | 0.073 | 0.96 | 0.27 | – | 0.42 | 0.015 | 0.21 | | 0.1 | ≤ 0.105 |
| 42CrMo | 1.0 | Bal. | | 0.2 | 0.25 | – | 0.80 | | | | 0.42 | – |

The electrorefining of spent nuclear fuels is performed under inert argon atmosphere partially in consideration of the highly hygroscopic nature of LiCl-KCl salt. In this work, all corrosion tests and salt preparations were conducted in an argon filled glove box in which the concentrations of moisture and oxygen in the argon atmosphere were controlled less than 1 ppm. LiCl (99% purity) and KCl (99.99% purity) salts were procured from Aladdin to prepare the LiCl-KCl eutectic salt using an analytical balance (Mettler, 10⁻⁴ g accuracy). Prior to corrosion testing, the salt mixture was dehydrated at 200 °C in an alumina crucible for 1 h. Then the salt was melted at 500 °C which is the typical operating temperature for the electrorefining of the metallic SNFs. Alloy specimens were fully immersed in the molten salt and tested for 500 h at 500 °C. After the corrosion test, alloy specimens were naturally cooled to room temperature, and the residual salt on the coupon surface was cleaned with deionized water and ethanol. For the liquid cadmium test, cadmium granules (99.99% purity) were melted in an alumina crucible also in the argon filled glove box. Alloy specimens were exposed to the liquid cadmium for 120 h at 500 °C.

A Zeiss GeminiSEM 500 scanning electron microscopy (SEM) equipped with an Oxford Ultim Max 50 energy dispersive spectroscopy (EDS) were employed to characterize the corrosion morphologies and chemical compositions of the corrosion products.

3. Results

3.1. Corrosion in molten LiCl-KCl eutectic

Moisture is the most common contaminant in consideration of the hydrophilic nature of chloride salt, which is also perhaps the most deleterious impurity in molten chloride salt. The moisture can react with chlorine ions in the salt to form highly corrosive hydrochloric acid according to reaction (1):



The accelerated corrosion of nickel and iron by the presence of moisture in the molten chloride media had been demonstrated in several studies [15-17]. Moreover, the moisture contamination also produces impurities of O^{2-} ions through reaction (1) which could alter the forms of corrosion products. The concentrations of O^{2-} ions can be referred to the salt basicity as defined by $pO^{2-} = -\log a_{O^{2-}}$. Metals can be corroded as soluble chlorides and/or solid oxides, depending on the electrode potential and the salt basicity. The thermodynamical stability domains of corrosion products can be illustrated by the E - pO^{2-} diagram. The calculated E - pO^{2-} diagrams for nickel, iron, chromium and molybdenum in molten LiCl-KCl salt at 500°C are given in Figure 1. The activities of MCl_n (M represents Ni, Fe, Cr and Mo) in the salt was assumed to 10^{-6} for the equilibrium calculations. The electrode potential was plotted versus Ag/AgCl by considering the correlation between the standard potential of Ag/AgCl with standard Cl_2/Cl^- potential in LiCl-KCl eutectic [18]. At sufficiently low concentrations of oxide ions impurities, metals are submitted to dissolution through chlorination reactions. Alloying elements that have high negative Gibb's free energy of chloride formation are more prone to active dissolution, i.e., $E_{Mo/MoCl_2} > E_{Ni/NiCl_2} > E_{Fe/FeCl_2} > E_{Cr/CrCl_2}$. With the increase of impurities of O^{2-} ions in the melt, formation of oxides of metals becomes thermodynamically favorable. As shown in Figure 1, oxides of Cr and Mo can be formed at much lower concentrations of O^{2-} ions compared to Ni and Fe oxides. More complicated, the oxide layer formed on the metal surface can also be dissolved by the basic fluxing mechanism in which case the oxide layer reacts with the O^{2-} and/or O_2 impurities to form soluble ternary products such as $LiCrO_2$ or $LiNiO_2$ [19,20]. The corrosion performance of alloys also largely depends on their chemical composition and microstructural characteristics (e.g., grain size, grain boundary, and the secondary precipitates). Therefore, there is a need to evaluate the corrosion performance of various alloys through corrosion testing.

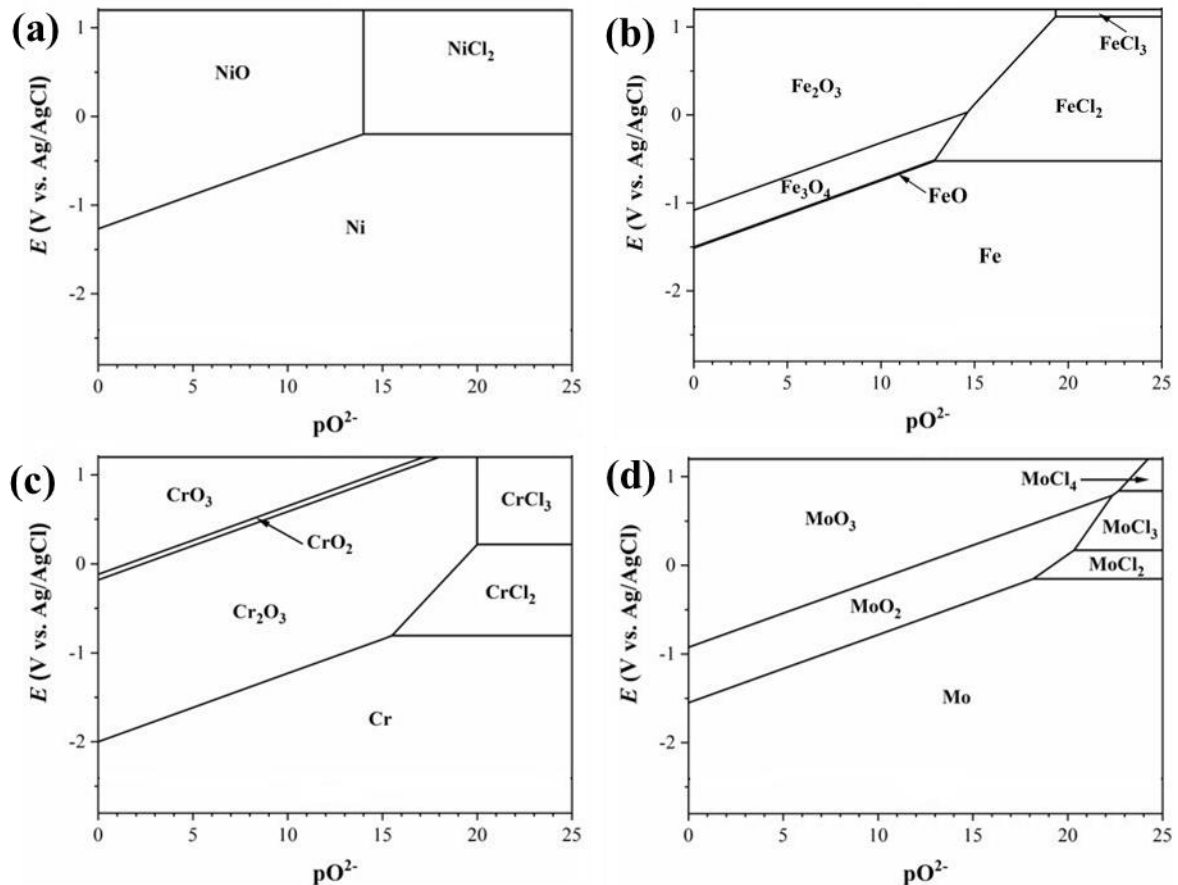


Figure 1. Calculated E - pO^{2-} diagram at 500°C for (a) Ni, (b) Fe, (c) Cr, and (d) Mo.

3.1.1. 42CrMo steel

42CrMo steel is a typical low-alloy, medium-carbon, high-strength steel, containing about 1 wt% Cr and 0.2 wt% Mo. Figure 2 shows the corrosion morphology of 42CrMo steel after 500 h of immersion in the molten LiCl-KCl salt at 500°C. The SEM surface micrograph in Figure 2a exhibits porous microstructure. The examination of the cross section revealed severely uneven steel surface with localized pitting attacks up to 10.2 μm depth (see Figure 2b). There is barely any oxide product on the steel surface as observed from the contrast of the backscattered electron image. However, the EDS elemental mapping manifests some oxygen enrichment at the steel surface, indicating the possible formation of oxide layer. The EDS point analysis did find some iron oxide islands on the steel surface, as evidenced by the composition of point 2 in Figure 2b. The two pits in Figure 2b are seemingly isolated from the steel surface, but they could be a 2-D side view of the sideways pits that have an undercutting or subsurface shapes. The EDS quantitative analysis of point 1 in the deep pit resulted in a composition of 60.41 at% Fe, 8.61 at% Cr and 30.99 at% O. This proves the presence of iron-chromium oxide products inside the pit. The EDS analysis of point 4 also indicates the formation of iron-chromium oxides inside the isolated pit. Therefore, these two pits were definitely formed through the corrosion process. They should have narrow openings which are not in the 2D cross-section in Figure 2b. Compared to the 1 wt% of Cr in the steel matrix, obvious chromium enrichment of the corrosion products inside the pits was evidenced. This should be attributed to the higher thermodynamic stability of chromium oxides (e.g., Cr₂O₃) compared to iron oxides (e.g., Fe₃O₄), as indicated by Figure 1. Moreover, the dissolution rate of oxide film inside the pit through the basic fluxing might be limited in consideration of the difficulty of inward diffusion of O²⁻ ions and O₂ from the bulk solution to the pit. Therefore, it is speculated that the formation of chromium oxides inside the pit may hinder the progression of pitting.

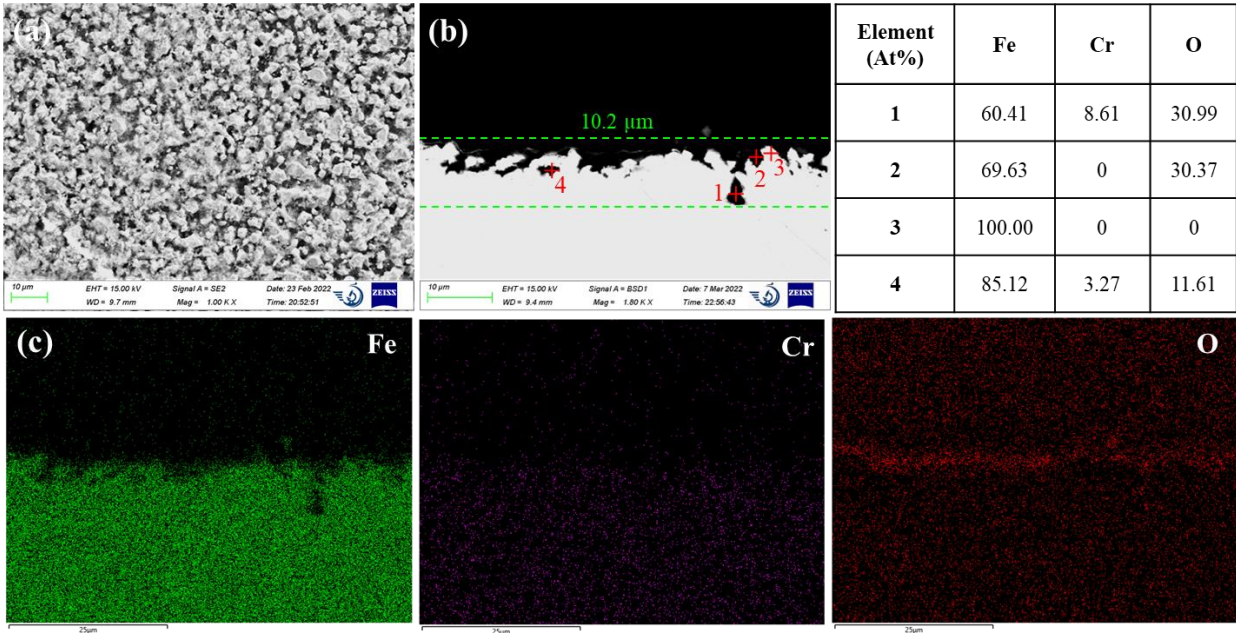


Figure 2. (a) SEM surface morphology of 42CrMo steel after 500 h corrosion in molten LiCl-KCl salt. (b) and (c) are the cross-sectional image and corresponding EDS elemental mapping.

3.1.2. AISI 316L

AISI 316L stainless steel is an austenitic chromium-nickel stainless steel that contains 16-18 wt% Cr, 10-14 wt% Ni, and 2-3 wt% Mo. Figure 3 shows the SEM micrographs and EDS analysis results of AISI 316L exposed for 500 h to the molten LiCl-KCl salt at 500°C.

AISI 316L exhibits a less uneven surface morphology compared to 42CrMo steel. Pieces of residual oxide scales can still be observed on the steel surface. The cross-sectional SEM image of AISI 316L shows a relatively uniform near-surface corroded layer with a thickness of 9.4 μm . The dissolution feature is in common with 42CrMo steel but more oxide islands are distributed in the pores of corroded near-surface region. The oxide islands are mainly composed of chromium oxides, as evidenced by the EDS quantitative analysis of points 1 and 2 in Figure 3b. Again, this suggests chromium oxides is more stable in molten chloride media than that of iron oxides. The residual steel matrix adjacent to the oxide islands in the near-surface corroded region contains less Fe and more Ni compared to the bulk steel matrix, as displayed by the EDS analysis results of points 3 and 4. This indicates iron is less resistant to dissolution than that of Ni, which can be attributed to the more negative chlorination potential of iron. Feng and Melendres [21] reported equilibrium potentials of -2.004 V versus Li^+/Li for Ni(II)/Ni and 1.590 V versus Li^+/Li for Fe(II)/Fe electrode reactions in molten LiCl-KCl eutectic at 450°C. Compared to 42CrMo steel, obvious pitting corrosion was not observed on AISI 316L. It is well known that the Mo addition increases the pitting corrosion resistance of stainless steels through two mechanisms [22]. One is the molybdenum oxide in the passive oxide film enhances the film stability. This might be not applicable in this case inconsideration of the porous and incomplete oxide film. The other effect of Mo is the inhibition of active dissolution kinetics after breakdown of the passive film. Here, Mo addition leads to the decrease of metastable pitting rate and size, thus retarding the development of metastable pit to stable pit. In addition, although AISI 316L manifests better resistance to pitting corrosion, severe intergranular attacks were observed on AISI 316L. As shown in Figure 3a, massive connected voids were concentrated at the grain boundaries. This might be attributed to the sensitization effect of stainless steel which is widely known to affect the intergranular corrosion behavior in aqueous solution. When austenitic stainless steel is heated in the sensitization temperature range between 450°C to 850°C for long time, chromium carbides can precipitate on the grain boundaries, leading to the depletion of Cr solute in the adjacent region. Thus, less chromium oxide products will be formed on the grain boundary surface which may make the grain boundary more susceptible to dissolution compared to the grain itself. The sensitization effect on the corrosion in molten chloride media had been previously reported by Polovov et al. [23] who studied the corrosion of austenitic stainless steel in molten NaCl-KCl salt. The resistance to intergranular corrosion was improved in the order of AISI 316L (< 0.03C, 2.2–2.8Mo, in wt%) > AISI 316Ti (< 0.1C, 0.5–0.7Ti, 2.0–3.0Mo, in wt%) > AISI 321 (< 0.12C, 0.5–0.8Ti, in wt%), due to the decreasing of the carbon content or increasing of the content of strong carbide forming elements.

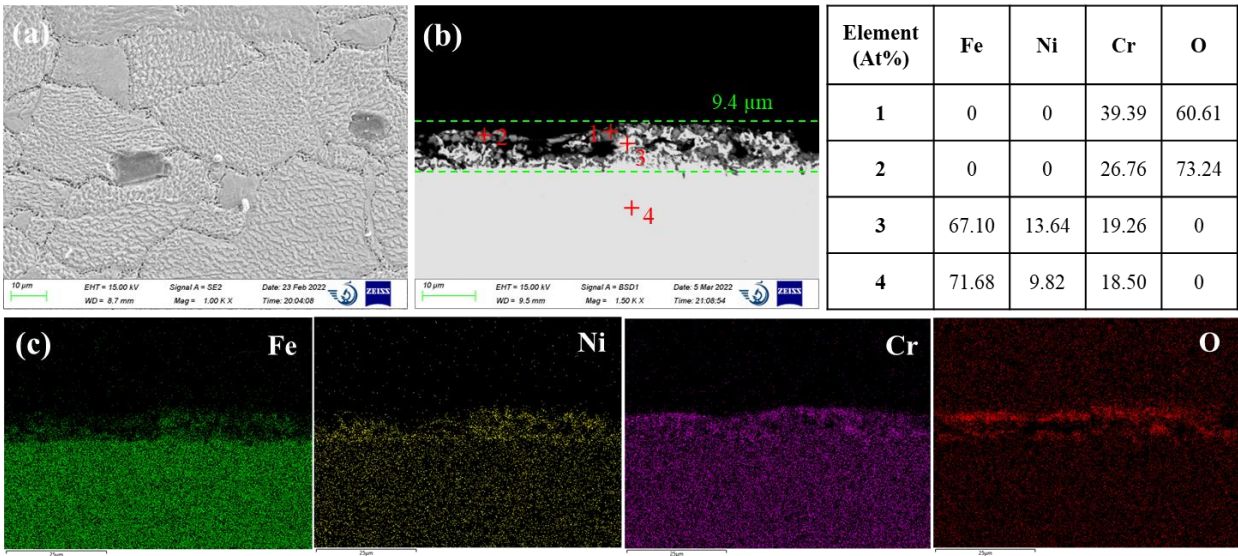


Figure 3. (a) SEM surface morphology of AISI 316L after 500 h corrosion in molten LiCl-KCl salt. (b) and (c) are the cross-sectional image and corresponding EDS elemental mapping.

3.1.3. Inconel 600

Inconel 600 is a nickel-chromium alloy with good oxidation resistance at higher temperatures. The high nickel content of the alloy enables it to retain considerable resistance to active dissolution under reducing conditions, while the addition of 14-17 wt% chromium content provides the alloy resistance to various oxidizing environments by forming passive oxide film. Figure 4 shows the representative SEM corrosion morphology of Inconel 600 specimen after 500 h of immersion in the molten LiCl-KCl salt. In general, there are many flocculent structure of corrosion products distributed in clumps on the surface. As indicated by the cross-sectional SEM image in Figure 4b, the entire surface is covered by an oxide layer with thickness in the range of 3 to 6 μm . The flocculent corrosion products are accumulated on the top of this oxide layer. Both the oxide layer and flocculent corrosion products are composed of chromium oxides with a little content of iron and nickel elements. Compared to the 72.79 at% Ni and 9.01 at% Fe in the alloy matrix (see EDS analysis of point 4 in Figure 4b), nickel and iron content in the oxide layer are obviously depleted. This indicates that even the relatively more electropositive nickel is dissolved in the molten chloride media through the chlorination reaction, i.e., Ni/NiCl_2 . In comparison, chromium is preferentially oxidized rather than to be chlorinated probably due to the stability of Cr_2O_3 at lower concentrations of O^{2-} (see Figure 1). Moreover, fluctuation of the alloy surface and some cavities below the oxide layer are observed from Figure 4b. This might be a precursor of localized attack that may occur when the alloy is exposed to the salt for longer time duration.

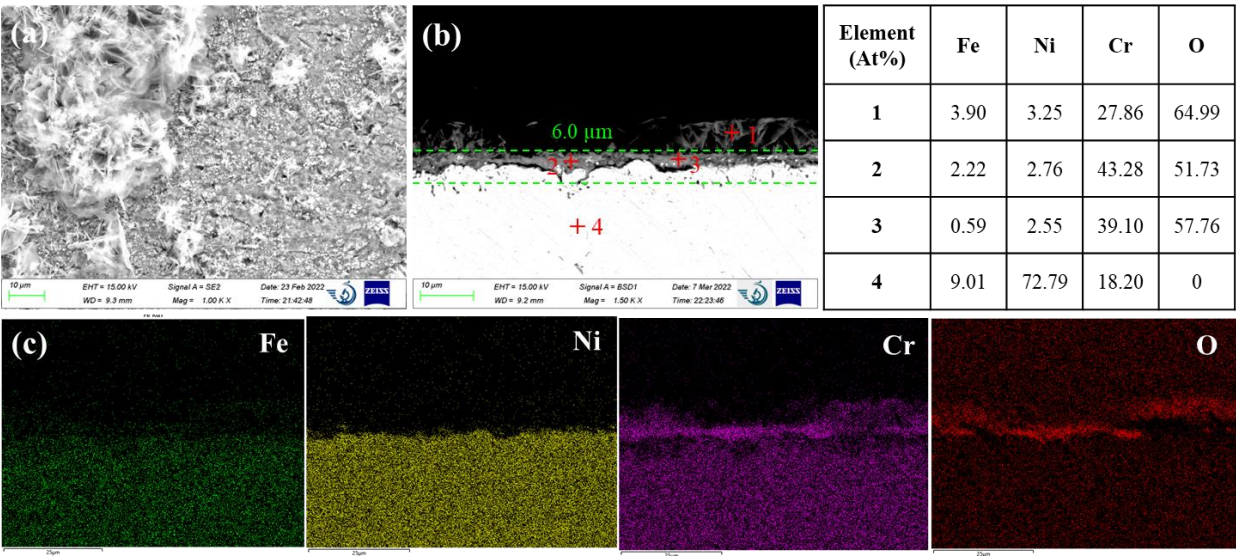


Figure 4. (a) SEM surface morphology of Inconel 600 after 500 h corrosion in molten LiCl-KCl salt. (b) and (c) are the cross-sectional image and corresponding EDS elemental mapping.

3.1.4. Haynes C276

Haynes C276 is a nickel-based superalloy with more than 50 wt% nickel, 15-17 wt% molybdenum and 14.5-16.5 wt% chromium. Haynes C276 exhibited a unique corrosion morphology compared to AISI 316L and Inconel 600, as shown in Figure 5. The SEM surface image demonstrated massive precipitates on the alloy surface. Examination of the cross section revealed a uniform oxide layer underneath these precipitates. Visually, there are still some light contrast alloy matrices remaining in the oxide layer. The EDS elemental mapping revealed that the oxide layer is enriched in Cr and O with presence of some Ni. The EDS quantitative analysis of points 2 and 3 exhibit an atomic ratio of Cr/O very close to Cr_2O_3 . The detected 10 – 13 at% of Ni in the thin oxide layer is probably associated to

the residual nickel matrix. The top precipitates are composited of more than 80 at% Ni and about 12–13 at% Fe. No molybdenum is detected either in the top precipitates or in the thin oxide layer. This suggests that Mo in the near-surface corroded region must be readily dissolved in the molten salt. However, Mo is more prone to chlorination than that of Ni and Fe. Thus, the depletion of Mo in the nickel matrix suggests that Mo was oxidized to volatile Mo oxides. In fact, formation of molybdenum oxides is thermodynamically favorable in salt with concentrations of O^{2-} ions as low as that for the formation of chromium oxides (see Figure 1). Amongst MoO_2 and MoO_3 , MoO_3 is more volatile at evaluated temperatures. The melting temperature of MoO_3 is $795^{\circ}C$, indicating a relatively high vapor pressure. Thus, it is speculated that Mo in the Haynes C276 was corroded through the formation of volatile MoO_3 . As Cr was also preferentially oxidized as Cr_2O_3 , remaining Ni and Fe were alloyed to form Ni-Fe precipitates in the near-surface corroded region. This suggests that the significant amounts of Mo addition in Haynes C276 might be detrimental as the evaporation of volatile Mo oxides could break down the chromium oxide layer and increase the dissolution rate of the alloy matrix underneath. Such effects had been previously reported by Shankar et al. [7] who found the corrosion rate of Inconel 625 (Ni-18Cr-4Fe-11Mo) was remarkably higher than Inconel 600 (Ni-17Cr-10Fe-1Mn) in molten LiCl-KCl eutectic due to the presence of Mo in Inconel 625.

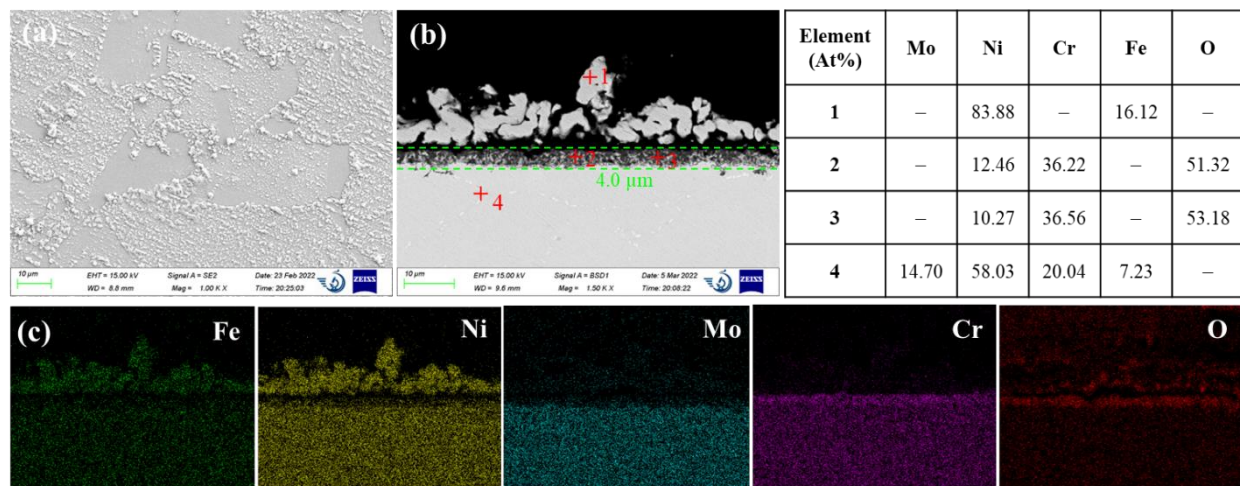


Figure 5. (a) SEM surface morphology of Haynes C276 after 500 h corrosion in molten LiCl-KCl salt. (b) and (c) are the cross-sectional image and corresponding EDS elemental mapping.

3.2. Corrosion in liquid cadmium

In liquid metals, corrosion of metal structure can proceed as a physical dissolution or chemical oxidation process, depending on the solubilities of alloying elements and the oxygen partial pressure in the system [12]. In low oxygen partial pressure conditions, the physical dissolution is predominated which is driven by the solubility of alloying elements in the liquid metal. For alloying elements of traditional corrosion resistance alloys, nickel is most soluble in liquid cadmium. According to the Ni-Cd phase diagram, the solubility of Ni in liquid Cd at $500^{\circ}C$ is more than 10 at% [11]. In comparison, Fe is almost insoluble in liquid Cd. Using a radiotracer technique Chasanov et al. [24] found solubilities of Fe in liquid Cd of 2.4×10^{-4} at% at 694 K and 4.4×10^{-1} at% at 920 K, respectively. The solubility of Cr in liquid Cd is also extremely low and values of 6.2×10^{-4} at% at 723 K and 37.3×10^{-1} at% at 923 K have been reported [24]. This indicates nickel-based alloys and nickel bearing steels may suffer the selective dissolution of nickel in the near-surface region. The dissolution may be accompanied with the penetration of cadmium into the alloy matrix, which could result in the alloy embrittlement widely known as the liquid metal embrittlement. When the oxygen partial pressure becomes higher than the saturated oxygen pressure for oxides, liquid metal corrosion may alter to chemical oxidation mechanism in which the oxidation kinetics is dependent on the oxygen partial pressure,

temperature, and mass transport in the alloy and liquid metal phases. The saturated oxygen pressures for Cr_2O_3 , Fe_3O_4 , NiO and CdO are in orders of 10^{-42} , 10^{-29} , 10^{-23} , and 10^{-25} atm at 500°C , respectively. In the electrorefining conditions, the concentration of oxygen impurities in the argon cover gas is typically controlled in the range of several to tens of ppm. Thus, formations of Cr_2O_3 , Fe_3O_4 , NiO and CdO are all thermodynamically possible. Therefore, it is necessary to investigate the corrosion mechanisms of structural materials in liquid cadmium.

3.2.1. AISI 316L

Figure 6 shows the cross-sectional SEM images and the corresponding EDS and XRD analysis results of AISI 316L stainless steel after 120 h of exposure in liquid cadmium at 500°C . The bright contrast in the backscattered electron image (Figure 6a and b) is the heavy metal cadmium that adheres on the steel surface. At the interface of 316L steel and cadmium, a uniform oxide layer with thickness of about $6 - 9\ \mu\text{m}$ was formed. Obviously, the protectiveness of this oxide layer is limited as the bright cadmium phase was embedded into the dark oxide layer, indicating the penetration of cadmium. Even for the dark oxide phase, the EDS quantitative analysis of point 2 and point 3 exhibits 12–18 at% of Cd. The XRD analysis of the corroded AISI 316L exhibited diffraction patterns associated to Fe_2O_3 and CdCrO_4 compounds (see Figure 6e). This is quite consistent with the EDS analysis results of points 2 and 3. Underneath the oxide layer, the penetration of Cd into the steel matrix up to a depth of about $11\ \mu\text{m}$ was also observed. This is very similar to the typical morphology of bismuth penetration into the austenitic stainless steels in liquid lead bismuth eutectic, which is caused by the depletion of high solubility of Ni in the near-surface region [25,26]. Here, the depletion of Ni is also identified from the EDS line scan in Figure 6d. As we mentioned, the solubility of Ni in liquid Cd at 500°C is more than 10 at%. Ni was also not detected in the oxide layer because formation of NiO is also thermodynamically less favorable than that of Cd, Fe, and Cr. Thus, Ni in the steel matrix must be readily dissolved in the liquid cadmium. This will lead to the transition of austenitic phase to ferritic phase as Ni is a key element for the stabilization of austenite, as acknowledged in the field of liquid lead bismuth corrosion [25,26]. Then liquid cadmium will penetrate into the Ni depleted region through the voids left by Ni and the grain boundaries of the fragmentized ferritic grains. In addition, sulfur oxide particles were observed outside the oxide layer surface. This indicates that sulfur impurities in the stainless steel was transferred to the liquid cadmium phase probably through the replacement reactions between Cd or CdO with the sulfide inclusions in the stainless steel such as FeS or MnS .

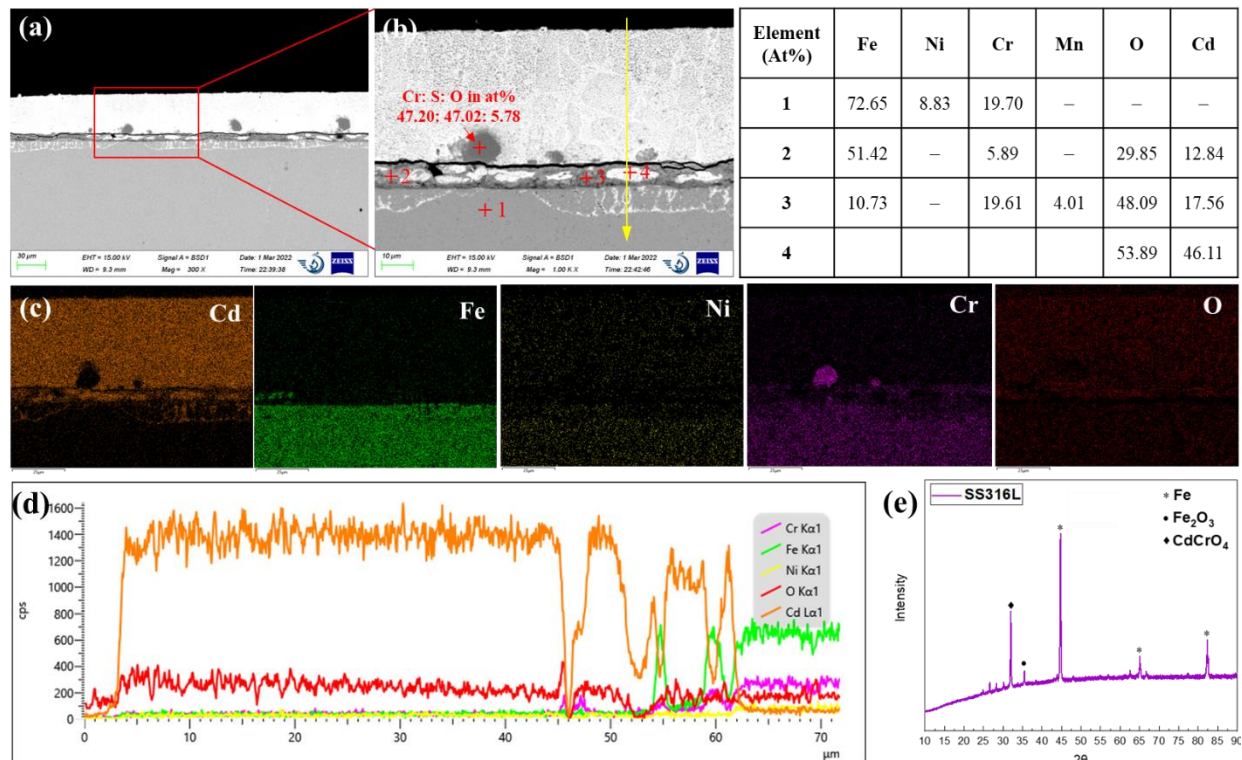


Figure 6. (a) and (b) SEM cross-sectional image and (c) the corresponding EDS elemental mapping of AISI 316 L after 120 h corrosion in liquid Cd; (d) EDS scan along the yellow line in (b); (e) XRD pattern.

3.2.2. T91 stainless steel

T91 is a martensitic Cr bearing stainless steel containing about 9 at% Cr and 1 at% Mo. As shown in Figure 7, T91 steel exhibited a bi-layer structure after exposed for 120 h in liquid cadmium. The outer layer with a darker contrast consists of Fe and O with an atomic ratio of Fe to O close to 1. The inner layer is enriched with more than 30 at% Cd, indicating the penetration of Cd. In addition to Cd, significant amounts of Fe, Cr and O were also detected. Similar to the oxide composition of AISI 316L, the inner oxide layer of T91 steel is also composed of Fe_2O_3 and CdCrO_4 . In fact, this is quite different from the typical bi-oxide layer structure observed on T91 steel in liquid lead bismuth eutectic which consists of an inner iron-chromium spinel oxide layer and an outer magnetite (Fe_3O_4) layer [13]. Compared to the protective inner spinel oxide layer in liquid lead bismuth conditions, the inner oxide layer formed in the liquid cadmium is quite reactive with Cd. It is speculated that Cd can diffuse through the outer iron oxide layer and react with the chromium oxide in the inner layer to form binary CdCrO_4 compound. Therefore, the corrosion of T91 martensitic steel in liquid cadmium is predominated by the chemical oxidation mechanism. Physical dissolution of alloying elements and penetration of Cd into the steel matrix is not obvious.

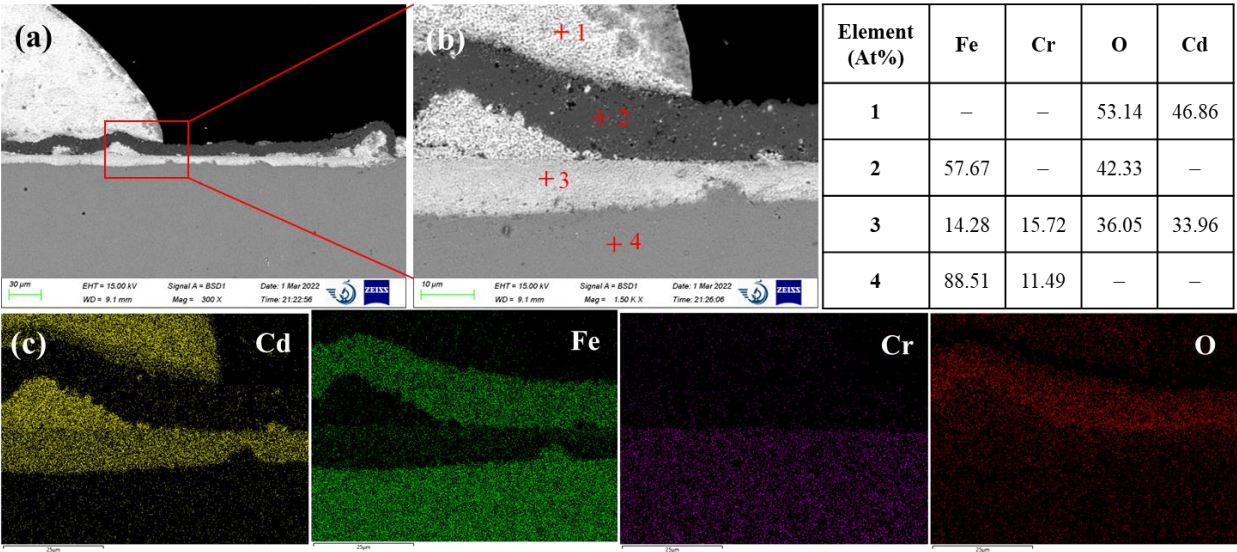


Figure 7. (a) SEM cross-sectional image, (b) the corresponding EDS elemental mapping and (c) EDS line scan of AISI 316 L after 120 h corrosion in liquid Cd.

3.2.3. Tungsten

To the authors’ knowledge, either the solubility data of tungsten in liquid cadmium or the binary phase diagram of W-Cd system is not available in literatures. Jang et al. [27] carried out the Cd distillation test from U-Cd alloy in a tungsten crucible at 500°C and found the tungsten crucible was very stable against Cd, maintaining a shiny surface, but the time duration was only 200 minutes for the Cd distillation test. This study further evaluated the compatibility of tungsten with cadmium in longer time duration. Figure 8 shows the corrosion morphology of pure tungsten after exposed for 120 h in liquid cadmium at 500°C. As tungsten is heavier than cadmium, it shows a brighter contrast in the backscattered electron image. The saturated oxygen pressures for tungsten oxides are equivalent with that of iron oxides, e.g., values of WO₂ and WO₃ at 500°C are in orders of 10⁻³¹ and 10⁻²⁹ atm. Thermodynamically, this means oxidation of tungsten is as favorable as iron. However, Figure 8 manifests no sign of oxidation of tungsten on the metal surface. Any chemical interaction between the tungsten and cadmium is also not observed. Hence, tungsten is quite chemically inert in liquid cadmium under argon atmosphere. Regarding to the physical dissolution, many residual fragments of tungsten are observed on the tungsten surface. Their chemical compositions are validated by the EDS analysis (see point 2). Depletion of tungsten in the near-surface region was also evidenced from the EDS line scan results in Figure 8d. Thus, it is obvious that the dissolution of tungsten was occurred in liquid cadmium. Conservatively, at least 6.8 μm thick tungsten was corroded in a duration of 120 h, corresponding to a dissolution rate of 0.50 mm/a.

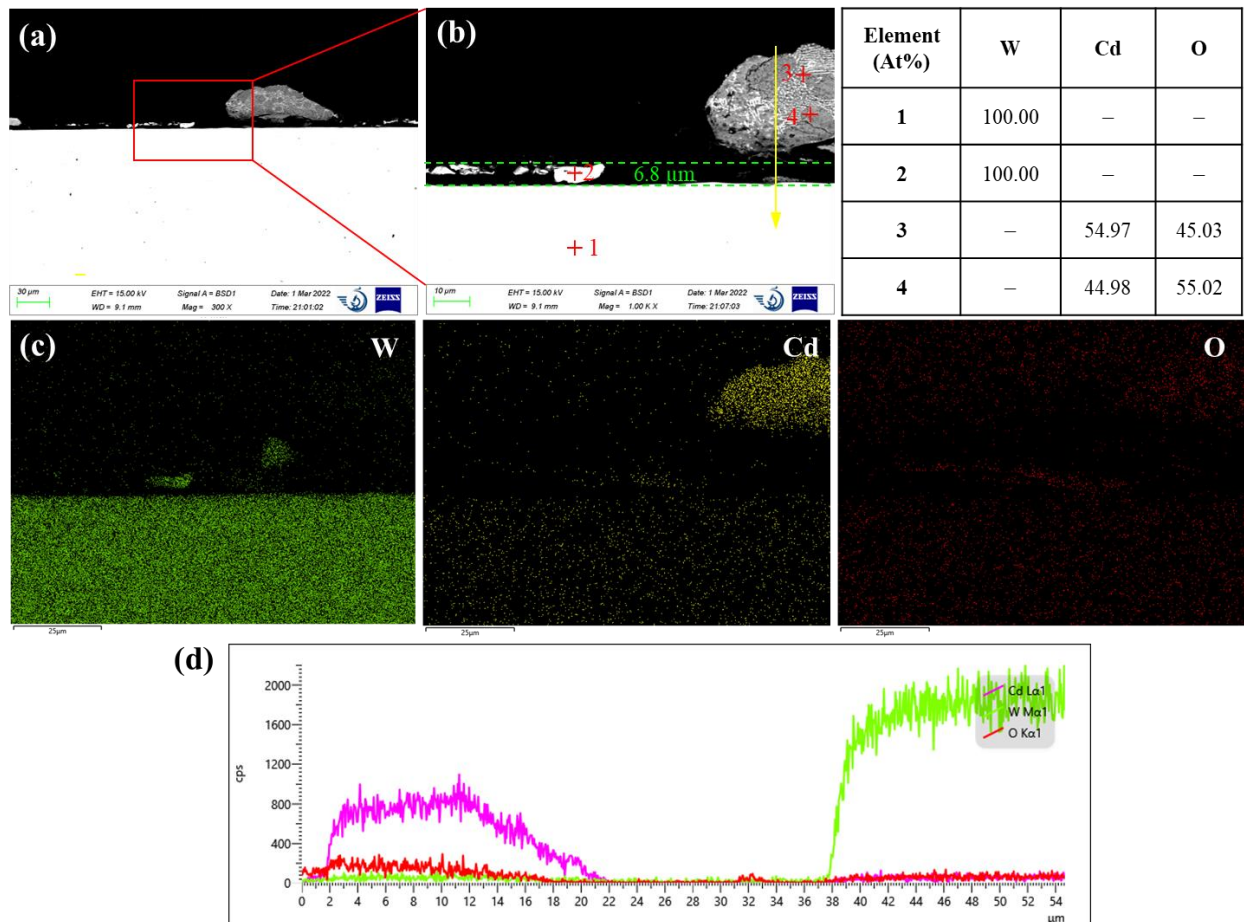


Figure 8. (a) and (b) SEM cross-sectional image and (c) the corresponding EDS elemental mapping of pure W after 120 h corrosion in liquid Cd, (d) EDS scan along the yellow line in (b).

5. Conclusions

42CrMo steel, AISI 316L, Inconel 600 and Haynes C276 were exposed to molten LiCl-KCl salt for 500 h at 500 °C under argon atmosphere. All test materials suffered active dissolution attacks, accompanied with the formation of porous oxide layer or oxide islands. 42CrMo and AISI 316L steels exhibited pitting and intergranular attacks respectively, while Inconel 600 showed less localized attack. The significant amount of Mo in the Haynes C276 accelerated the dissolution rate probably due to the formation of volatile Mo oxides, resulting in the Ni-Fe precipitates in the corroded region.

AISI 316L in liquid cadmium suffered from both the dissolution of Ni and chemical oxidation of Fe and Cr, while the corrosion of T91 stainless steel was predominated by chemical oxidation. Cd can permeate into the oxide layer and react with chromium oxide to form CdCrO_4 . The dissolution of Ni in AISI 316L resulted in the penetration of Cd into the steel matrix to depth of 11 μm . In comparison, tungsten only suffered from physical dissolution with rate of more than 0.50 mm/a.

Author Contributions: Conceptualization, S.G.; methodology, S.G. and Y.J.; formal analysis, S.C.; investigation, S.C., Y.J. and X.D.; writing—original draft preparation, S.G. and Y.J.; writing—review and editing, S.G.; supervision, S.G.; funding acquisition, S.G. All authors have read and agreed to the published version of the manuscript.

Funding: Please add: This research was funded by Natural Science Basic Research Program of Shaanxi Province, grant number 2022JQ372”.

Data Availability Statement: The data presented in this study are available on request from the corresponding author. The data are not publicly available due to privacy.

Acknowledgments: The authors wish to thank Mr. Zijun Ren at Instrument Analysis Center of Xi'an Jiaotong University for his assistance with SEM analysis. Special thanks to Mr. Jiong Qian at Jiuli Hi-Tech Metals for providing the Haynes C276, Inconel 600, and AISI 316L alloy bars.

Conflicts of Interest: The authors declare no conflict of interest.

References

- [1] M.A. Williamson, J.L. Willit, Pyroprocessing flowsheets for recycling used nuclear fuel, *Nucl. Eng. Technol.*, **2011**, 43, 329-334.
- [2] S. Guo, J. Zhang, W. Wu, W. Zhou, Corrosion in the Molten Fluoride and Chloride Salts and Materials Development for Nuclear Applications. *Prog. Mater. Sci.*, **2018**, 97, 448-487.
- [3] E. V. Nikitina, N. A. Kazakovtseva, E. A. Karfidov, Corrosion of 16Cr12MoWSVNbB (EP-823) Steel in the LiCl-KCl Melt Containing CeCl₃, NdCl₃ and UCl₃. *J. Alloys Compd.*, **2019**, 811, 152032.
- [4] E. A. Karfidov, E. V. Nikitina, Corrosion Electrochemical Behavior of Nickel in the LiCl-KCl Melt Containing Lanthanum Trichloride. *Russ. Metall.*, **2019**, 8, 820-824.
- [5] S. Guo, W. Zhuo, Y. Wang, J. Zhang, Europium Induced Alloy Corrosion and Cracking in Molten Chloride Media for Nuclear Applications, *Corros. Sci.*, **2020**, 163, 108279.
- [6] A. R. Shankar, S. Mathiya, K. Thyagarajan, U. Kamachi Mudali, Corrosion and Microstructure Correlation in Molten LiCl-KCl Medium. *Metall. Mat. Trans. A*, **2010**, 41, 1815-1825.
- [7] A. R. Shankar, A. Kanagasundar, U. K. Mudali, Corrosion of Nickel-Containing Alloys in Molten LiCl-KCl Medium. *Corrosion*, **2013**, 69, 48-57.
- [8] A.R. Shankar, K.Thyagarajan, U. K. Mudali, Corrosion Behavior of Candidate Materials in Molten LiCl-KCl Salt under Argon Atmosphere. *Corrosion*, **2013**, 69, 655-665.
- [9] C. J. Rao, A. R. Shankar, P. K. Ajikumar, M. Kamruddin, C. Mallika, U. K. Mudali, Corrosion Behavior of Structural Materials in LiCl-KCl Molten Salt by Thermogravimetric Study. *Corrosion*, **2015**, 71, 502-509.
- [10] S. Chang, Y. Jia, X. Du, S. Guo, Corrosion Behavior of Commercial Alloys in LiCl-KCl Molten Salt Containing EuCl₃, *Front. Mater.*, **2022**, 9, 958296.
- [11] B. Predel, Cd-Ni (Cadmium-Nickel), In *Phase Equilibria, Crystallographic and Thermodynamic Data of Binary Alloys · Ca-Cd – Co-Zr*, O. Madelung, Eds.; SpringerMaterials: Verlag Berlin Heidelberg, 1993; pp. 1-3.
- [12] J. Zhang, N. Li, Review of the studies on fundamental issues in LBE corrosion, *J. Nucl. Mater.*, **2008**, 373, 351-377.
- [13] J. Zhang, A review of steel corrosion by liquid lead and lead-bismuth, *Corros. Sci.*, **2009**, 1207-1227.
- [14] X. Gong, M.P. Short, T. Auger, E. Charalampopoulou, K. Lambrinou, Environmental degradation of structural materials in liquid lead- and lead-bismuth eutectic-cooled reactors, *Prog. Mater. Sci.*, **2022**, 126, 100920.
- [15] Y. Hosoya, T. Terai, T. Yoneoka, S. Tanaka, Compatibility of structural materials with molten chloride mixture at high temperature, *J. Nucl. Mater.*, **1997**, 248, 348-353.
- [16] F. Colom, A. Bodalo, Corrosion of Iron (ARMCO) in KCl-LiCl Melts, *Corros. Sci.*, **1973**, 12, 731-7388.
- [17] A. Nishikata, H. Numata, T. Tsuru, Electrochemistry of molten salt corrosion, *Mater. Sci. Eng. A*, **1991**, 146, 15-31.
- [18] S. P. Fusselman, J. J. Roy, S. L. Grimmer, Thermodynamic Properties for Rare Earths and Americium in Pyropartitioning Process Solvents, *J. Electrochem. Soc.*, **1999**, 146, 2573-2580.
- [19] W. Phillips, D. Chidambaram, Corrosion of stainless steel 316L in molten LiCl-Li₂O-Li, *J. Nucl. Mater.*, **2019**, 517, 241-253.
- [20] R.Y. Liu, X. Wang, J.S. Zhang, X.M. Wang, Corrosion of nickel in molten LiCl-Li₂O at 750 °C, *J. Nucl. Mater.*, **2004**, 327, 194-201.
- [21] X.K. Feng, C. A. Melendres, Anodic Corrosion and Passivation Behavior of Some Metals in Molten LiCl-KCl Containing Oxide Ions, *J. Electrochem. Soc.*, **1982**, 129, 1245-1249.
- [22] Y.-T. Sun, X. Tan, L.-L. Lei, Y.-M. Jiang, Revisiting the effect of molybdenum on pitting resistance of stainless steels, *Tungsten*, **2021**, 3, 329-337.
- [23] I. B. Polovov, A. V. Abramov, O. I. Rebrin, V. A. Volkovich, E. I. Denisov, T. R. Griffiths, I. May, H. Kinoshita, *ECS Trans.* **2010**, 33, 321-327.
- [24] M. G. Chasanov, P. D. Hunt, I. Johnson, H. M. Feder, Solubility of 3-d transition metals in liquid cadmium, *Trans. Met. Soc. AIME*, **1962**, 224, 935.
- [25] C. Schroer, O. Wedemeyer, J. Novotny, A. Skrypnik, J. Konys, Selective leaching of nickel and chromium from Type 316 austenitic steel in oxygen-containing lead-bismuth eutectic (LBE), *Corros. Sci.*, **2014**, 84, 113-124.
- [26] P. Hosemann, D. Frazer, E. Stergar, K. Lambrinou, Twin boundary-accelerated ferritization of austenitic stainless steels in liquid lead-bismuth eutectic, *Scr. Mater.*, **2016**, 118, 37-40.
- [27] J. Jang, S. Han, T.-J. Kim, G.-Y. Kim, C. H. Lee, S.-J. Lee, Stability of Tungsten Crucible against Uranium, Rare Earth, Cadmium, and Chlorides for Cathode Process in Pyroprocessing, *Sci. Technol. Nucl. Install.*, **2019**, 2019, 4121285.